A&A 389, 977–992 (2002)
DOI: 10.1051/0004-6361:20020397

Astronomy & Astrophysics

Results of the SEST Key Programme: CO in the Magellanic Clouds

VIII. The giant molecular complex No. 37 of the LMC⋆

G. Garay[1], L. E. B. Johansson[2], L.-Å. Nyman[3], R. S. Booth[2], F. P. Israel[4], M. L. Kutner[5], J. Lequeux[6], and M. Rubio[1]

[1] Departamento de Astronomía, Universidad de Chile, Casilla 36-D, Santiago, Chile
[2] Onsala Space Observatory, 439 92 Onsala, Sweden
[3] European Southern Observatory, Casilla 19001, Santiago 19, Chile
[4] Sterrewacht, Postbus 9513, 2300 Leiden, The Netherlands
[5] NRAO, 949 N. Cherry Av., Campus Building 65, Tucson, Arizona 85721-0655, USA
[6] DEMIRM, Observatoire de Paris, 61 Av. de l'Observatoire, 75014 Paris, France

Received 29 November 2001 / Accepted 12 March 2002

Abstract. We report observations of the CO(1→0), CO(2→1) and ^{13}CO(1→0) line emission from the giant molecular complex No. 37 of the Large Magellanic Cloud, made with linear resolutions between 6 and 12 pc. The observations were undertaken with the Swedish-ESO Submillimetre Telescope (SEST) as part of the Key Programme: CO in the Magellanic Clouds. We find that the CO(1→0) emission arises from six large, distinct, molecular clouds, with CO luminosities in the range 1×10^4 to 5×10^4 K km s^{-1} pc^2 and sizes between 22 and 38 pc, and seven smaller clumps, with CO luminosities in the range between 7×10^2 and 2×10^3 K km s^{-1} pc^2. The opacities in the CO(1→0) line at the peak position of the large clouds are remarkably smaller than those derived for Galactic molecular clouds. Relationships between line width, size and CO luminosities are discussed. The total CO luminosity of the complex determined from the SEST observations, of 1.8×10^5 K km s^{-1} pc^2, is in excellent agreement with that determined from the low spatial resolution (∼140 pc) observations of Cohen et al. On the other hand, the total mass of molecular gas in the complex derived from the SEST observations, assuming that the individual clouds are virialized, is 2.4×10^6 $M_\odot$, which is a factor of 6 lower than that estimated by Cohen et al. under the same assumption. We conclude that the value of the velocity integrated CO emission to H_2 column density conversion factor in the LMC determined from low angular resolution observations has been overestimated by a factor of ∼3. We derive a conversion factor for clouds in Complex-37 of $\sim 6 \times 10^{20}$cm^{-2} K^{-1} km^{-1} s, which is similar to that for clouds in the outer Galaxy.

Key words. galaxies: Magellanic Clouds – ISM: clouds – ISM: molecules – radio lines: ISM

1. Introduction

The Magellanic Clouds provide unique opportunities for studying molecular clouds and star formation in galaxies whose environment is very different from that of the Milky Way. In particular, in the Large Magellanic Cloud (LMC) the metallicity is a factor of 2–3 times lower than in our Galaxy (Garnett 1999) and the gas-to-dust ratio is four times the Galactic value (Koornneef 1982). In addition the far-UV radiation field, which strongly affects the properties of molecular clouds, is more intense than in the Galaxy and shows large variations across the LMC (Lequeux 1989). Cohen et al. (1988) first surveyed the CO(1→0) line emission from the LMC, with an angular resolution of 8′.8 (∼140 pc at the distance of 55 kpc), identifying forty-one giant molecular complexes within the LMC. The complexes have, typically, radii of ∼180 pc and line widths of ∼11 km s^{-1}.

Over the last decade the SEST telescope has been used to map, with tenfold higher angular resolution than in the previous survey, a few of the complexes within the LMC. The purpose of these observations is to determine the structure and kinematics of the giant molecular clouds at linear resolutions of ∼10 pc, and relate their observed characteristics to the properties of the environment and to the presence of energy sources (eg., HII regions, SNR's, etc.). It is hoped that these observations will provide answer to questions such as: Is the emission coming from a relatively small number of giant molecular clouds (GMCs), with extents of tens of parsecs, as in the Milky Way, or is there a higher proportion of smaller clouds? How is the

Send offprint requests to: G. Garay,
e-mail: guido@das.uchile.cl

⋆ Based on results collected at the European Southern Observatory, La Silla, Chile.

difference in metallicity and gas-to-dust ratio reflected in the properties of molecular clouds? Is the conversion factor from CO luminosities to masses of molecular clouds different than in our Galaxy?

In this paper we report the results of CO and ^{13}CO line observations, made with SEST, of the giant molecular complex No. 37 (hereafter Complex-37) in the catalog of Cohen et al. (1988). This complex was selected because it is associated with moderate activity of massive star formation. Results of observations of CO emission from molecular complexes associated with either regions which do not show signs of high mass star formation or in the vicinity of regions with strong activity of massive star formation have been reported by Kutner et al. (1997; Paper VI) and Johansson et al. (1998, Paper VII), respectively. Observations of neutral hydrogen toward Complex-37 show the presence of two distinct HI components with LSR velocities of about 232 and 276 km s^{-1} (Rohlfs et al. 1984; Luks & Rohlfs 1992). Even though the two HI clouds have relatively similar intensities, – the brightness of the lower velocity component is a factor of 2 higher than that of the high velocity component –, the CO survey of Cohen et al. (1988) shows emission only from the low velocity component. The higher resolution of the SEST observations will provide more adequate data to establish the relationship between the HI and CO emission.

2. Observations

The observations of the CO(1→0), CO(2→1) and ^{13}CO(1→0) line emission from Complex-37 were made during six periods from December 1992 to December 1994 using the Swedish-ESO Submillimetre Telescope (SEST) located on La Silla, Chile. The telescope beam size at the frequencies of the CO(1→0) and CO(2→1) lines are 43″ and 24″ (*FWHM*), respectively. In the 3 mm wavelength range the receiver was a single channel cooled Schottky mixer, tuned to be optimized as a single sideband receiver. In the 1.3 mm wavelength range the receiver was an SiS receiver. Single-sideband receiver temperatures were typically 500 and 400 K for the low and high frequency receivers, respectively. The back end was an acousto-optical spectrometer, which provided 2000 channels with a spectral resolution of 43 kHz/channel.

The observations in the CO(1→0) line were performed as follows. First, we made a complete unbiased mapping of an area of 24′ × 24′ with 60″ spacings, in the position switch mode. The goal was to obtain an unbiased census of the molecular material in this complex. We observed 454 positions which fully covered the region of Complex-37 as observed by Cohen et al. (1988) with 8.′8 angular resolution. The 2000 channel spectrometer, which was centered at the LSR velocity of 260 km s^{-1}, provided a velocity resolution of 0.11 km s^{-1} and a velocity coverage of 225 km s^{-1}. The integration time on source at each position was 3 min, resulting in an rms noise in a single spectral line channel of typically 0.14 K. Hereafter we will refer to this mapping as the survey. Thereafter, and in order to better determine their spatial structure, we made full maps with 20″ spacings across the clouds detected in the survey. These observations were made in a frequency switching mode, with a throw of 15 MHz. The line was always in the spectrometer bandpass for both halves of the switching cycle. Spectra were folded in the final processing to improve the rms by $\sqrt{2}$. In overall we observed 974 positions, with integration times on source of 3 min, which resulted in an rms noise of typically 0.13 K.

The ^{13}CO(1→0) line emission was mapped, with 60″ spacings, across regions of the survey where CO(1→0) emission was detected. In total we observed 63 positions. The observations were performed in the position switch mode using two dual polarization mixers. The rms noise in a single spectral line channel, achieved after an integration time on source of 10 min, was typically 0.035 K. The CO(2→1) line emission was mapped, with 20″ spacings, across a fraction of the clouds detected in the survey. We observed, in the position switch mode, a total of 275 positions with integration times on source of 3 min, which resulted in an rms noise of typically 0.18 K. Finally, we supplement the above data with observations of the CS(2→1) line, undertaken with the SEST during October 1993 and January 1996, toward four positions which correspond to peak positions of clouds identified in the survey. The integration times were typically 120 min, which resulted in an rms noise of typically 0.013 K.

Intensity calibration was performed using the chopper technique, in which the receiver alternatively looks at the sky and an ambient temperature absorber during the calibration phase. The time between calibrations was typically 10 min. The intensities are reported as $T_{\rm A}^*$ (Kutner & Ulich 1981), in which the intensities are corrected for atmospheric attenuation and rear ward spillover. To convert to $T_{\rm mb}$, the brightness temperature for a source that uniformly fills the main beam, one must divide $T_{\rm A}^*$ by the main beam efficiency, $\eta_{\rm mb}$. We used $\eta_{\rm mb} = 0.73$ at 98 GHz, 0.70 at 115 GHz, and 0.60 at 230 GHz. Unless otherwise stated, contour maps and spectra are presented on the $T_{\rm A}^*$ scale. Tabulated properties, such as peak temperature or integrated intensity, as well as derived quantities, such as CO luminosities, will be presented on the $T_{\rm mb}$ scale, since we are talking about objects for which there is some idea of the extent relative to the beam size. Pointing was checked periodically on the SiO maser, R Dor, which is near the LMC in the sky. This allowed pointing checks in the same azimuth and elevation range as the source. The rms pointing errors were typically 4″ in each axis.

3. Results

3.1. CO(1→0) and ^{13}CO(1→0) emission with 60″ spacings

Figure 1 shows the line profiles of the CO(1→0) emission from a region of 24′×24′, with 60″ spacings, covering the whole area of Complex-37 (the survey). The offsets are with respect to $\alpha(1950) = 5^{\rm h}45^{\rm m}24\overset{\rm s}{.}5$, $\delta(1950) = -69°34'0''$. The emission from Complex-37 as

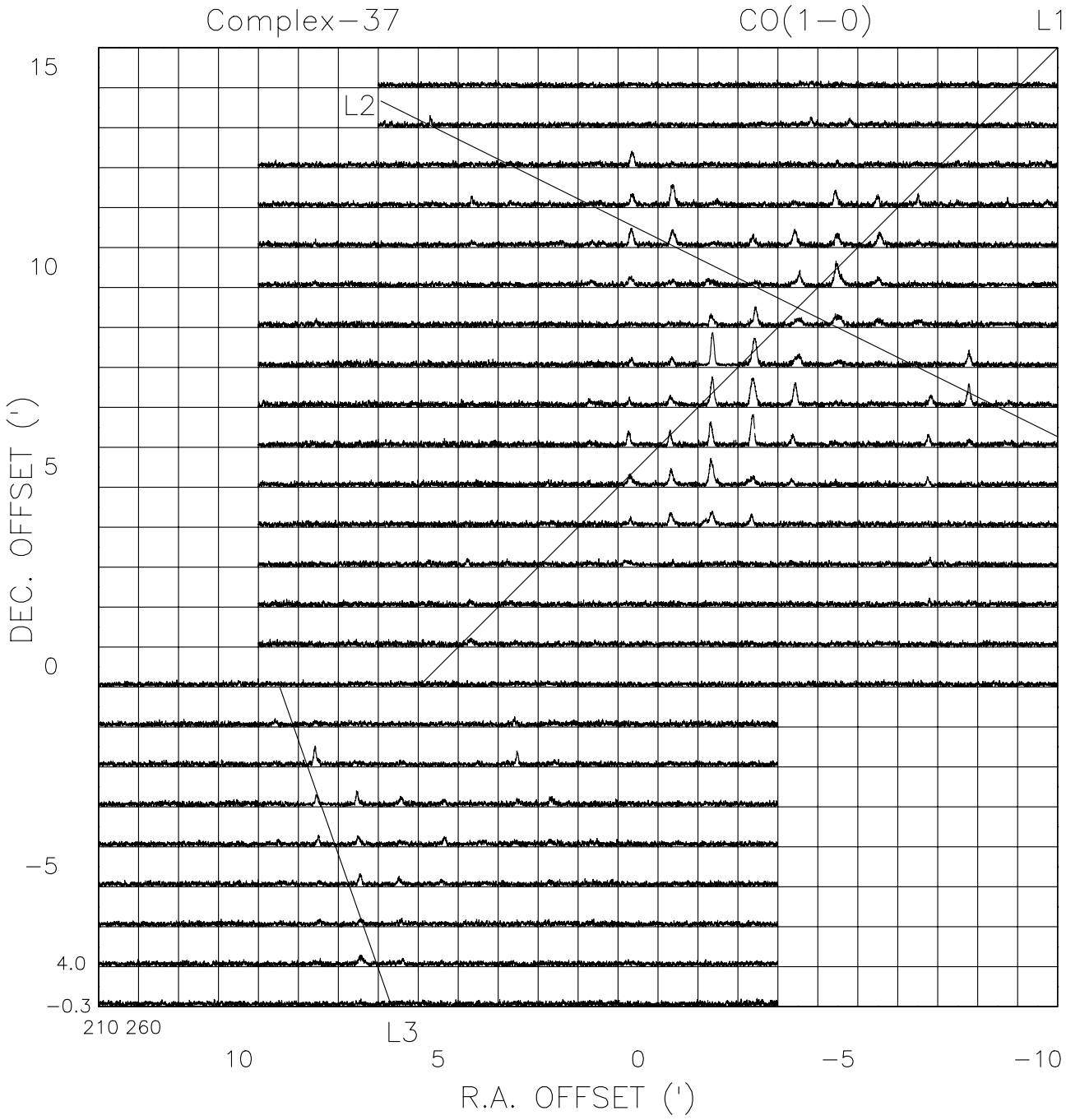

Fig. 1. Spectra of the CO(1→0) emission from a $24' \times 24'$ region of the LMC encompassing Complex-37. The grid spacing is $1'$. Offsets are from the reference position at $\alpha_{1950} = 5^{\rm h}45^{\rm m}24\overset{\rm s}{.}5$, $\delta_{1950} = -69°34'0''$. The velocity scale is from 210 to 260 km s^{-1} and the antenna temperature scale is from −0.3 to 4.0 K. The lines indicate the directions of the $p - v$ diagrams presented in Fig. 11.

observed with SEST arises from a region that covers only about 22% of the total area subtended by the complex as seen with $8\overset{'}{.}8$ angular resolution. Of the 454 positions observed, emission above our threshold of 0.42 K (=3σ rms noise level) was found in 102 positions. Most of the emission comes from a region of $\sim 12'$ in diameter, located toward the northwest of the mapped area. No emission was found at velocities close to those of the 276 km s^{-1} HI component.

In order to separate the emission into individual clouds, we present in Fig. 2 contour maps of the CO(1→0) emission integrated in velocity intervals of 1.5 km s^{-1} over successive velocity ranges, from 219.5 to 255.5 km s^{-1}. Further in our efforts to isolate individual clouds, we produced images of the velocity integrated CO(1→0) line emission, line center velocity, and velocity dispersion across the region by computing moments of the line flux density, using the AIPS task XMOM. These images and

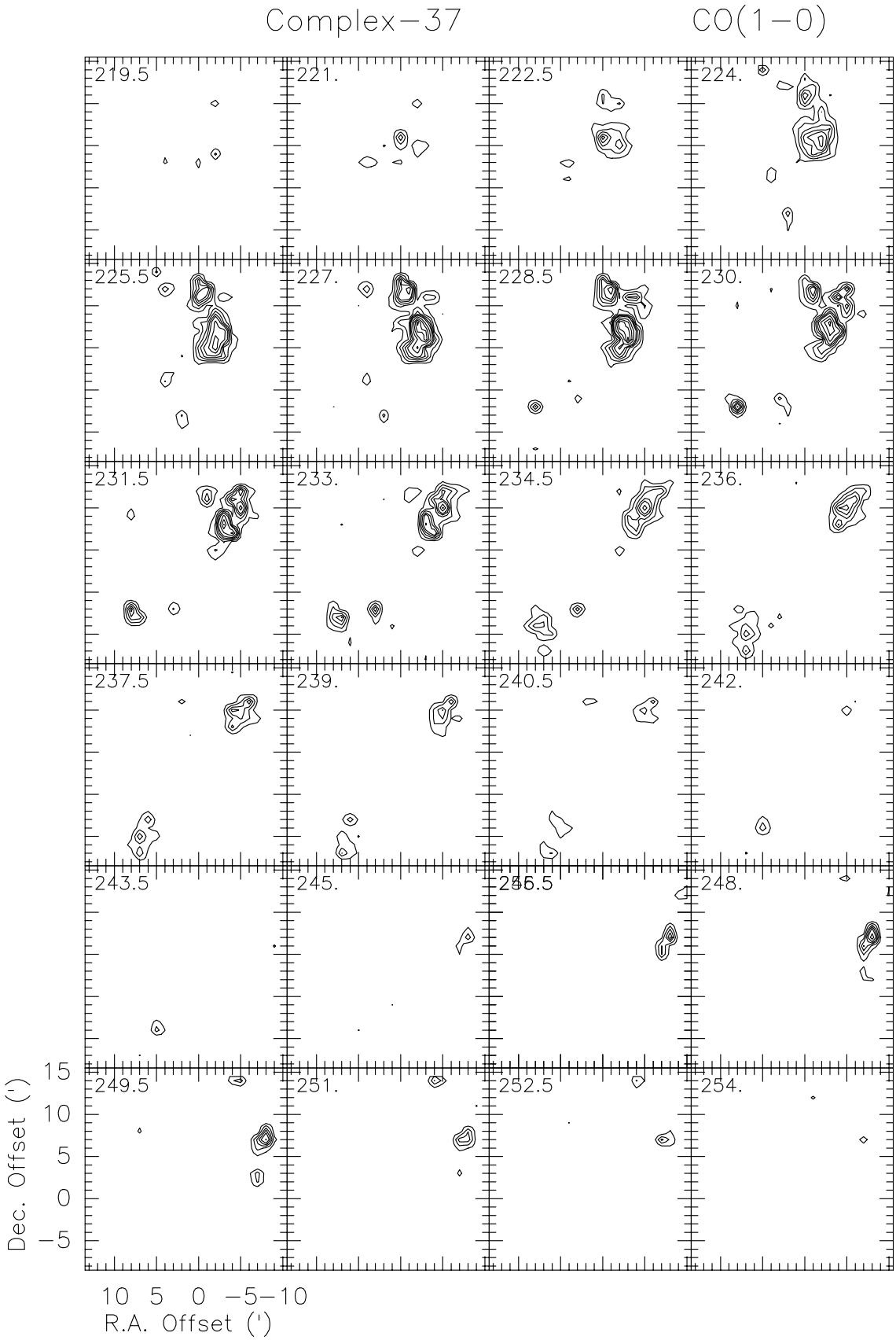

Fig. 2. Line maps of the CO(1→0) emission from Complex-37. The velocity width is 1.5 km s^{-1}. The initial LSR velocity, in km s^{-1}, is indicated at the top left corner of each line map. Contour levels are $\{-1, 1, 2, 3, 4, 5, 7, 9, 11, 13,$ and $15\} \times$ 0.35 K km s^{-1}. The (1σ) rms noise in the line maps is 0.10 K km s^{-1}.

Table 1. Observed parameters.

Name	Peak position		R	L_{CO}
	α(1950)	δ(1950)	(pc)	(K km/s pc^2)
	Clouds			
A	$05^h43^m54^s.74$	$-69°26'53''.7$	22	1.0×10^4
B	05 44 28.56	−69 23 59.4	31	3.3×10^4
C	05 44 52.47	−69 26 39.1	31	5.2×10^4
D	05 45 0.42	−69 29 6.3	35	3.5×10^4
E	05 45 15.58	−69 22 26.1	24	2.0×10^4
F	05 46 55.92	−69 36 4.9	38	2.2×10^4
	Clumps			
1	05 44 3.22	−69 31 15.6	13	1.1×10^3
2	05 44 36.22	−69 19 55.3	13	1.7×10^3
3	05 45 57.42	−69 35 52.0	16	1.9×10^3
4	05 46 10.51	−69 32 44.5	16	2.4×10^3
5	05 46 9.47	−69 22 10.0	13	1.4×10^3
6	05 46 23.99	−69 19 44.4	9	7.3×10^2
7	05 46 55.72	−69 24 43.6	16	1.1×10^3

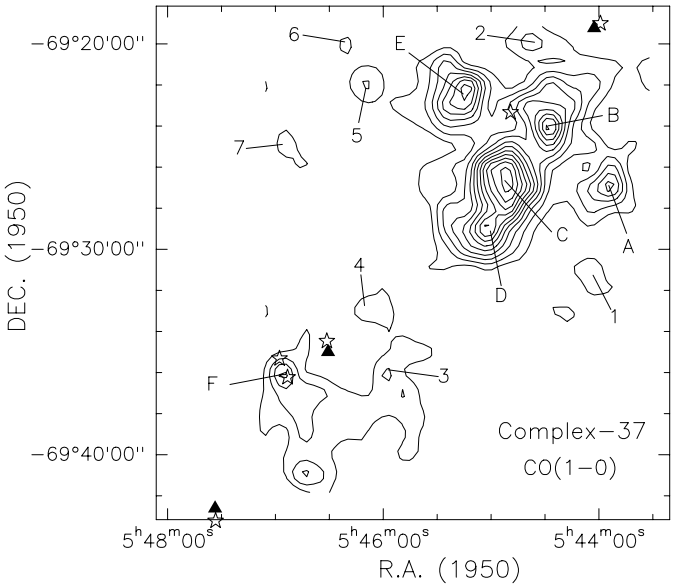

Fig. 3. Map of the integrated CO(1→0) emission from Complex-37. The range of velocity integration is from 221 to 254 km s^{-1}. The lowest contour and contour interval is 1.7 K km s^{-1}.

Fig. 2 show that the emission is coming from structures that are distinctly localized in position and velocity. Based on the continuity of the CO(1→0) emission both in position and velocity, we identify six large molecular structures (hereafter referred as clouds; labeled with capital letters A through F) and seven smaller structures (hereafter referred as clumps; labeled with numbers 1 through 7). The spatial location and extent of the clouds and clumps are shown in Fig. 3 which presents a contour map of the velocity integrated CO emission. Five of the six large molecular clouds (clouds A, B, C, D, and E) appear close together, lying within a region of ∼100 pc in radius. The peak position of the clouds and clumps are given in Cols. 2 and 3 of Table 1. When applicable, the radii and CO luminosities in this table come from the fully sampled observations described in Sect. 3.2, otherwise from the under-sampled observations described in the present Section. The triangles in Fig. 3 indicate the peak position of the three radio continuum sources cataloged by Filipovic et al. (1995) within the observed region. The southeast source (MC 89 in the catalog of McGee et al. 1972) has been identified as a supernova remnant (Mathewson et al. 1983; Dickel & Milne 1994), whereas the other two objects have spectral indices consistent with that of an optically thin thermal source and therefore can be identified as HII regions. The stars in Fig. 3 indicate the peak position of the six Hα+N[II] objects detected, within the mapped region, by Davies et al. (1976; hereafter DEM sources). Three of them (Nos. 304, 312, and 316), which are also the most extended objects, are associated with the radio continuum sources. The other three (Nos. 307, 313, and 314) are compact (knots) and lay projected within the contours of the CO emission.

The first order moment (mean velocity) image, presented in Fig. 4, allows us to investigate the global velocity field within the whole region and also to look for systematic velocity structure, such as rotation or expansion, within the individual clouds. This image strikingly shows a considerable range in the mean velocity of clouds and clumps. The most redshifted velocities (∼250 km s^{-1}) are exhibited by clumps 1 and 2, while the most blue shifted velocities (∼225 km s^{-1}) are exhibited by clumps 4 and 6. Figure 4 also shows the presence of significant velocity structure within some of the clouds. Cloud F exhibits a shift in the central velocity in a direction with a position angle of ∼−20°, increasing from ∼230 km s^{-1} in the northeast edge to ∼239 km s^{-1} in the southwest edge. The velocity field of cloud B shows fluctuations from point to point, having a more turbulent appearance than the other clouds. On the other hand, clouds A and E show little velocity structure across their faces; their line center velocities being approximately constant. The clumps also show approximately nearly constant line center velocities, except for clump 3 which shows two well defined velocities.

Figure 5 shows a map of the ^{13}CO(1→0) velocity integrated emission from the top region of Complex-37, observed with 60″ spacings. The morphology and velocity structure of the ^{13}CO emission is similar to that of the ^{12}CO emission.

3.2. CO(1→0) and CO(2→1) emission with 20″ spacings

Figure 6 shows maps of the velocity integrated CO(1→0) line emission from the top and bottom regions of Complex-37 observed with 20″ spacings. The top region covers the emission from clouds A, B, C, D, and E, whereas the bottom region the emission from cloud F and clumps 3 and 4. The clouds defined in the survey with 60″ spacings still appear as distinct units, spatially

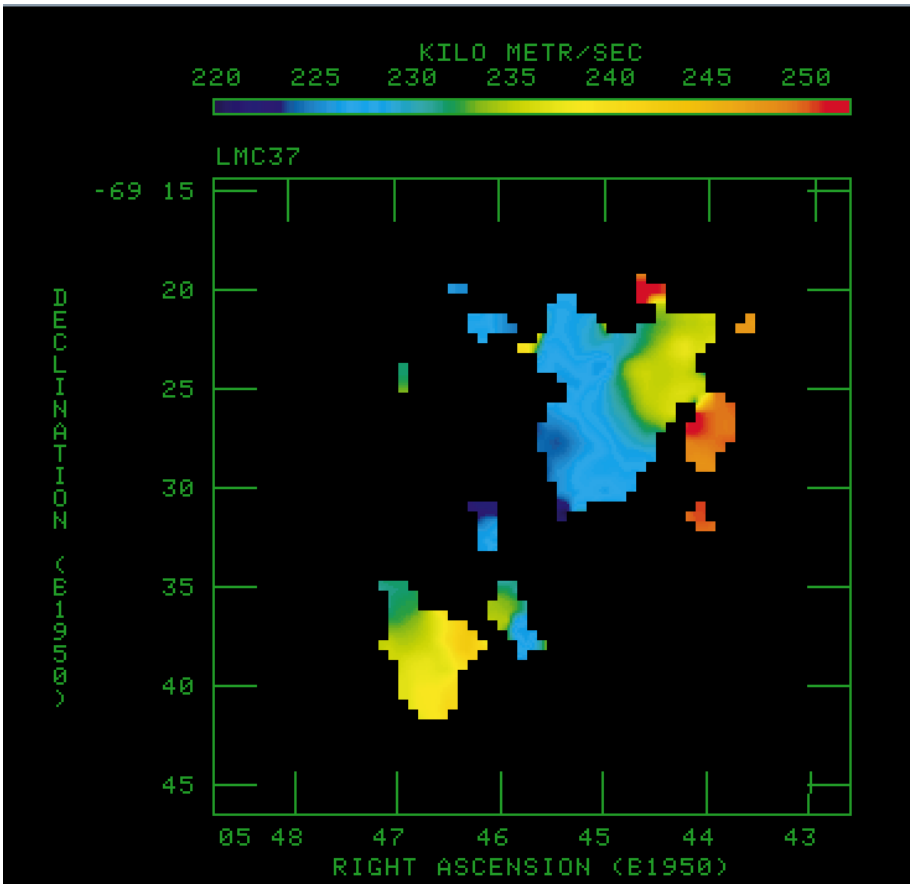

Fig. 4. Color image of the mean velocity of the CO(1→0) emission from clouds and clumps within Complex-37. The velocity-color code is shown in the top, with velocity ranging from 220 to 254 km s^{-1}.

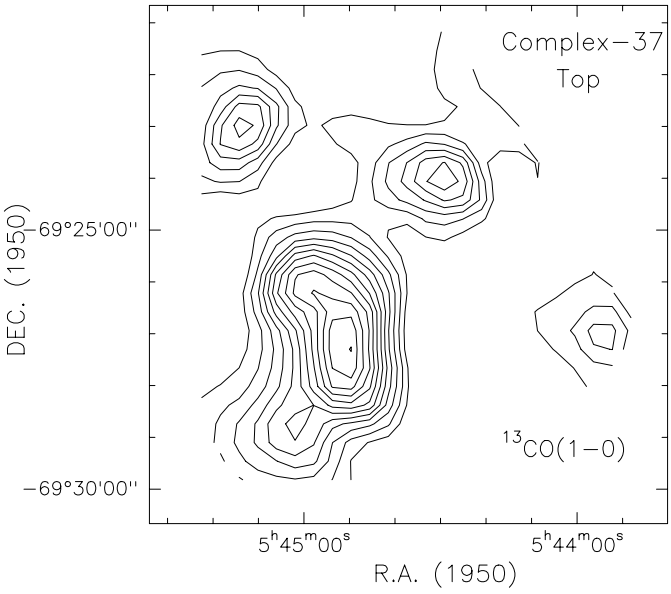

Fig. 5. Map of the integrated ^{13}CO(1→0) emission from the top region of Complex-37. The range of velocity integration is from 221 to 254 km s^{-1}. The lowest contour and contour interval are 0.4 and 0.2 K km s^{-1}, respectively.

and kinematically, when observed with 20″ spacings, although the latter observations show finer details in the morphology and velocity structure within each cloud. For instance, cloud C exhibits two peaks separated by ∼1′.2. The observed spatial-velocity distribution does not, however, indicate the presence of two distinct, independent clouds. Cloud F exhibits an irregular, multiple peaked, morphology, with the strongest peak located near the northeast border. Its emission is considerably weaker than that from clouds in the top region. Figure 7 presents a map of the velocity integrated CO(2→1) emission from the top region taken with 20″ spacings. Note that the mapped region covers cloud A and partially clouds B, C and D. The shape of the profiles in the CO(1→0) and CO(2→1) lines do not show significant differences. This is illustrated in Fig. 8, which shows the peak and integrated spectra of the CO(1→0) and CO(2→1) line emission from cloud A. The ratio of CO(2→1) to CO(1→0) brightness temperature across the whole region mapped in CO(2→1) span a narrow range, from 0.80 to 1.24, with an average value of 1.0.

3.3. Observed parameters

The line parameters of the integrated emission from the six clouds and seven clumps identified within Complex-37 are given in Table 2. The average brightness, line center velocity, line width, and average velocity integrated main-beam brightness temperature ($\int T_{\rm mb}\, {\rm d}v$) are given,

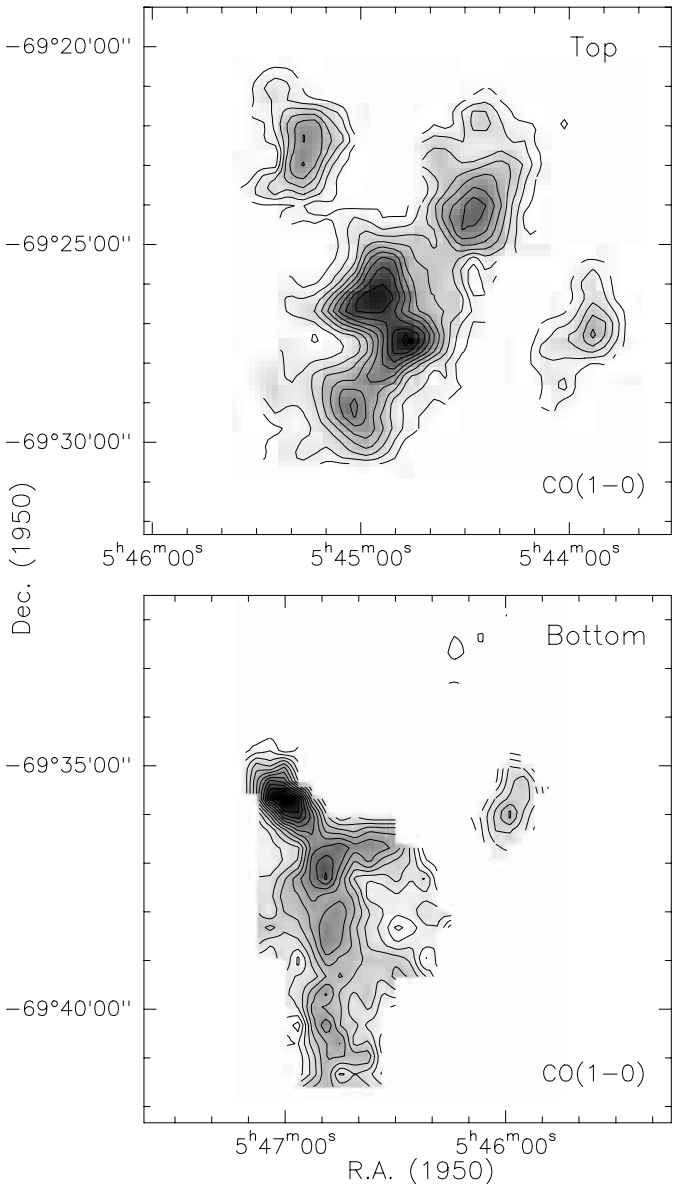

Fig. 6. Maps of the velocity integrated CO(1→0) emission from Complex-37, obtained using the 20″ spacing observations. Upper panel: top region. Velocity integration range: 221 to 254 km s^{-1}. The lowest contour and contour interval is 2.2 K km s^{-1}. Lower panel: bottom region. Velocity integration range: 224 to 244 km s^{-1}. The lowest contour and contour interval is 0.7 K km s^{-1}.

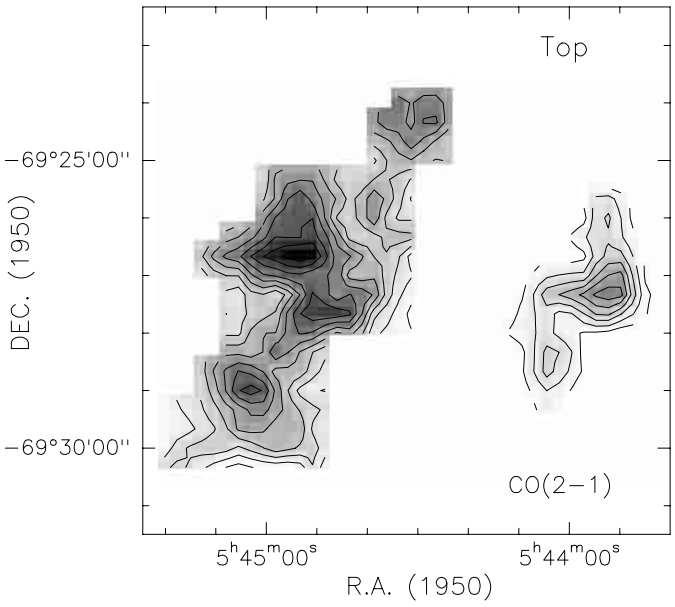

Fig. 7. Map of the velocity integrated CO(2→1) emission from the top region of Complex-37, obtained with 20″ spacing observations. The lowest contour and contour interval is 2.0 K km s^{-1}.

respectively, in Cols. 2 to 5 for the CO(1→0) emission and in Cols. 6 to 9 for the ^{13}CO(1→0) emission. The parameters were determined from Gaussian fits to the composite spectrum shown in Fig. 9.

The line parameters of the CO(1→0), CO(2→1), ^{13}CO(1→0), and CS(2→1) emission determined from Gaussian fits to the observed spectra at the peak position of the clouds, shown in Fig. 10, are given in Table 3. The peak main beam brightness temperature of the CO(1→0) line emission is typically 3 K, the strongest value being 5.8 K (cloud C). The CO lines are weaker by a factor of ∼5 than those expected from a typical Milky Way cloud complex if moved at the distance of the LMC and observed with a resolution of 10 pc (Kutner et al. 1997). The difference in line strengths suggests that one or more of the physical conditions that affect line intensities are different in the LMC-Complex-37 and the Milky Way. Possible factors affecting the strength of the lines in the LMC involves lower CO abundance, which would produce lower CO column densities and therefore weaker CO lines, and/or lower kinetic temperatures and densities which would result in lower excitation temperatures and hence weaker lines. Low excitation temperatures and densities would produce CO(2→1)/CO(1→0) line intensity ratios smaller than 1, contrary to the results of Table 2, and can be excluded. The most likely explanation is that the molecular gas in LMC clouds fills a smaller fraction of the volume than in the Milky Way, and therefore the emission is weaker due to the smaller filling factors. This hypothesis has been proposed by Rubio et al. (1993) and developed by Lequeux et al. (1994) (respectively Papers III and IV of this series) to account for similar properties of the molecular clouds in the Small Magellanic Cloud. It is supported by observations of CII emission which show that the molecular clumps in the LMC have larger C^+ envelopes relative to CO than those in our Galaxy (Mochizuki et al. 1994; Israel et al. 1996). The lower dust abundance in the LMC allows UV photons to penetrate deeper into the clumps than in our Galaxy, causing the CO clumps to shrink. Note that in this picture H_2 is also expected to be partly dissociated in the inter-clump medium, so that the clouds contain atomic hydrogen in addition to H_2. We designate these (likely) composite structures as "molecular clouds".

The observed cloud radius, given in Col. 4 of Table 1, is defined as $R = \left(\frac{N}{\pi}\right)^{1/2} \Delta s$, where Δs is the linear grid

Table 2. Line parameters of integrated emission.

Name	CO(1 → 0)				^{13}CO(1 → 0)			
	$T_{\rm mb}$ (K)	$V_{\rm LSR}$ (km s^{-1})	Δv (km s^{-1})	$\int T_{\rm mb}{\rm d}v$ (K km s^{-1})	$T_{\rm mb}$ (K)	$V_{\rm LSR}$ (km s^{-1})	Δv (km s^{-1})	$\int T_{\rm mb}{\rm d}v$ (K km s^{-1})
Clouds								
A	1.24	249.1 ± .03	5.29 ± .07	6.96 ± .09	0.13	248.9 ± .1	4.31 ± .24	0.613 ± .029
B	1.18	234.5 ± .04	9.48 ± .09	11.9 ± .1	0.073	234.3 ± .2	9.74 ± .37	0.753 ± .029
C	2.74	228.9 ± .01	6.19 ± .03	18.0 ± .07	0.26	229.1 ± .03	5.78 ± .08	1.59 ± .01
D	1.51	226.4 ± .02	6.67 ± .05	10.8 ± .07	0.12	226.4 ± .07	5.85 ± .18	0.767 ± .01
E	1.71	228.0 ± .03	6.41 ± .07	11.7 ± .10	0.16	227.6 ± .06	5.28 ± .16	0.901 ± .029
F	0.48	236.1 ± .07	10.0 ± .15	5.1 ± .07	–	–	–	–
Clumps								
1	0.81	250.1 ± .07	2.58 ± .17	2.21 ± .11	–	–	–	–
2	0.77	251.3 ± .09	4.30 ± .22	3.53 ± .16	–	–	–	–
3	0.87	234.1 ± .07	2.87 ± .19	2.64 ± .14	–	–	–	–
	0.38	230.3 ± .16	2.95 ± .33	1.19 ± .13	–	–	–	–
4	0.42	224.9 ± .16	7.38 ± .31	3.31 ± .13	–	–	–	–
6	1.12	225.5 ± .06	2.53 ± .14	3.01 ± .14	–	–	–	–
7	0.37	231.3 ± .14	3.88 ± .33	1.54 ± .11	–	–	–	–

spacing (in our case 5.3 or 16 pc) and N is the number of positions at which the cloud is detected. The CO luminosity, $L_{\rm CO}$, defined as $L_{\rm CO} \equiv < \int T_{\rm mb}\ {\rm d}v > N(\Delta s)^2$, is given in Col. 5 of Table 1.

Ratios of peak ($T_{\rm mb}$) and velocity integrated ($\int T_{\rm mb}{\rm d}v$) line intensities observed at the peak position of the clouds within Complex-37 are presented in Cols. 2 to 7 of Table 4. Column 8 of Table 4 gives the ratio of ^{12}CO and ^{13}CO line intensities integrated over velocity and angular extent of each cloud ($\int\int T_{\rm mb}{\rm d}v{\rm d}\Omega$).

4. Discussion

The most immediate result of our SEST observations is that the CO emission from Complex-37 comes from well defined clouds, with sizes ranging from 9 to 38 pc. The sum of the CO luminosities of the clouds observed with SEST, of 1.8×10^5 K km s^{-1} pc^2, is in excellent agreement with the luminosity measured with the 1.2-m CTIO telescope of 2.0×10^5 K km s^{-1} pc^2. We conclude that the weak main beam brightness temperatures of the CO emission from Complex-37 observed with the CTIO telescope, of ∼0.2 K, are mainly due to beam dilution effects (cf. Rubio & Garay 1988). There is no evidence for the presence of an extended (≥50 pc), optically thin, emission component of low brightness which could have also explained the weakness of the emission as observed with the CTIO telescope. CO is probably almost absent in the diffuse medium, as is H_2 (Tumlinson et al. 2001). In this section we discuss the characteristics of the molecular emission from clouds and clumps and the derivation of their physical parameters.

4.1. Molecular masses

Masses can be estimated assuming that the clouds are in virial equilibrium. For spherical clouds the virial mass, $M_{\rm vir}$, is given by

$$M_{\rm vir} = B \left(\frac{R}{\rm pc}\right) \left(\frac{\Delta v}{\rm km\ s^{-1}}\right)^2 M_\odot, \quad (1)$$

where B is a constant which depends on the density profile of the cloud and in the above units is 210 for a uniform density sphere and 190 for one whose density varies as the inverse first power of the radius (MacLaren et al. 1988). Masses computed from Eq. (1), using $B = 190$, are given in Col. 2 of Table 5.

The total mass of "molecular" gas, or more exactly of gas in the molecular clouds since some of this gas is likely to be atomic, in Complex-37 derived from the SEST observations, assuming that the individual clouds are virialized, is $2.4 \times 10^6\ M_\odot$, which is a factor of six smaller than that estimated by Cohen et al. (1988) under the same assumption. The large values of the virial masses estimated in the latter work are most likely due to the low angular resolution of their observations, which cause an overestimate of cloud radius and line width.

Another method to estimate molecular cloud masses is from the observed CO luminosity. Assuming that the H_2 column density, $N(H_2)$, is proportional to the velocity integrated CO emission, $N(H_2) = X \int T_{\rm mb}{\rm d}v$, integration over the solid angle subtended by the cloud, gives

$$M_{\rm CO} = 6.09 \left(\frac{X}{2.8 \times 10^{20}\ {\rm cm^{-2}\ K^{-1}\ km^{-1}\ s}}\right) \left(\frac{\mu}{2.72\, m_{\rm H}}\right) \times \left(\frac{L_{\rm CO}}{\rm K\ km\ s^{-1}\ pc^2}\right) M_\odot, \quad (2)$$

Table 3. Line parameters of emission at peak position[a].

Cloud	Line	$T_{\rm mb}$ (K)	$V_{\rm LSR}$ (km s^{-1})	Δv (km s^{-1})	$\int T_{\rm mb}{\rm d}v$ (K km s^{-1})
A.....	CO(1 → 0)	3.29 ± .17	249.4 ± .03	4.85 ± .06	16.99 ± .19
	CO(2 → 1)	4.08 ± .35	249.2 ± .03	5.21 ± .07	22.67 ± .28
	^{13}CO(1 → 0)	0.37 ± .04	249.1 ± .08	3.87 ± .17	1.54 ± .06
	CS(2 → 1)	0.063 ± .010	248.9 ± .15	4.36 ± .30	0.29 ± .01
B[b].....	CO(1 → 0)	2.93 ± .17	233.7 ± .07	5.39 ± .14	16.80 ± .47
	CO(2 → 1)	2.82 ± .23	233.5 ± .04	6.13 ± .10	18.40 ± .25
	^{13}CO(1 → 0)	0.21 ± .04	233.6 ± .01	6.42 ± .46	1.50 ± .09
	CS(2 → 1)	0.027 ± .016	233.6 ± .01	4.38 ± 2.3	0.125 ± .04
	CO(1 → 0)	1.41 ± .17	239.7 ± .13	4.82 ± .32	7.27 ± .50
	CO(2 → 1)	2.15 ± .23	239.7 ± .03	3.02 ± .10	6.92 ± .22
C.....	CO(1 → 0)	5.76 ± .16	228.6 ± .01	4.93 ± .03	30.16 ± .17
	CO(2 → 1)	4.62 ± .32	228.2 ± .02	5.27 ± .06	25.92 ± .27
	^{13}CO(1 → 0)	0.68 ± .04	228.4 ± .04	4.02 ± .10	2.90 ± .06
	CS(2 → 1)	0.090 ± .012	228.2 ± .13	4.62 ± .29	0.45 ± .027
D.....	CO(1 → 0)	3.83 ± .17	226.8 ± .02	5.62 ± .06	22.91 ± .20
	CO(2 → 1)	3.93 ± .25	227.0 ± .03	6.24 ± .07	26.18 ± .25
	^{13}CO(1 → 0)	0.29 ± .04	227.0 ± .01	5.94 ± .30	1.80 ± .09
E.....	CO(1 → 0)	3.10 ± .21	228.6 ± .04	5.83 ± .09	19.19 ± .26
	^{13}CO(1 → 0)	0.26 ± .04	228.0 ± .11	4.04 ± .26	1.13 ± .06
	CS(2 → 1)	0.048 ± .021	228.6 ± .42	5.05 ± .73	0.26 ± .04
F.....	CO(1 → 0)	2.43 ± .21	231.1 ± .05	4.31 ± .13	11.13 ± .26
	^{13}CO(1 → 0)	0.19 ± .04	231.4 ± .16	3.92 ± .37	0.80 ± .07

[a] Errors are formal 1σ values for the model of a Gaussian line shape.
[b] Two Gaussian components fitted to the CO(1→0) and CO(2→1) profiles.

where $m_{\rm H}$ is the mass of a hydrogen atom and μ is the mean molecular weight per H_2 molecule (=2.72 $m_{\rm H}$ when He is taken in account). The constant of proportionality X is an entirely empirical quantity whose value and constancy from place to place, cloud to cloud, and galaxy to galaxy have been much debated. For clouds in our Galaxy the conversion factor has been determined by several methods. Here we use for comparison the conventional value $X_{\rm G} = 2.8 \times 10^{20}$ cm^{-2} K^{-1} km^{-1} s (Scoville & Sanders 1987; Strong et al. 1988; Combes 1991) although more recent determinations point to somewhat lower values (Digel et al. 1996, 1999; Hunter et al. 1997; Dame et al. 2001). However, due to the lower metallicity, lower dust abundance, and higher UV interstellar radiation field of the LMC than in our Galaxy, the conversion factor for the LMC is likely to be different than the Galactic value, and therefore the $M_{\rm CO}$ masses computed assuming $X = X_{\rm G}$ may not be suitable. We find that the CO masses of the Complex-37 clouds computed using the conventional Galactic conversion factor are in average a factor of 2.3 times smaller than the virial masses. This suggests that the conversion factor toward Complex-37 is 2.3 times larger than the conventional Galactic value, or $X = 6.4 \times 10^{20}$ cm^{-2} K^{-1} km^{-1} s. This value is in excellent agreement with that obtained by Israel (1997) toward this region of the LMC, from an analysis of the far-infrared surface brightness and HI column density. Masses computed from Eq. (2), using $X = 2.3\ X_{\rm G}$, are given in Col. 3 of Table 5. We note that since the total CO luminosity of Complex-37 measured with the SEST and Columbia telescopes are in agreement, the total CO mass derived for Complex-37 is the same for both data sets, regardless of the value of X used.

The mass of a molecular cloud can, in addition, be estimated through observations of an optically thin transition, which allows a direct estimate of the mass in the observed species. The total mass is then inferred assuming an appropriate abundance ratio. The mass computed in this way is usually called the LTE mass, since typically only one transition is measured and an extrapolation to the total column density is done assuming a local thermodynamic equilibrium (LTE) population. For ^{13}CO the LTE mass is given by (cf. Bourke et al. 1997)

$$\left(\frac{M_{\rm LTE}}{M_\odot}\right) = 0.312 \left(\frac{\mu}{2.7\, m_{\rm H}}\right) \left(\frac{[{\rm H_2}/^{13}{\rm CO}]}{7\times10^5}\right) \left(\frac{D}{\rm kpc}\right)^2 \times \left\{\frac{T_{\rm ex}+0.88}{1-\exp(-5.29/T_{\rm ex})}\right\} \iint \tau_{13}{\rm d}v{\rm d}\Omega, \quad (3)$$

where μ is the mean molecular mass per H_2 molecule, $m_{\rm H}$ is the mass of a hydrogen atom, D is the source distance, v is in km s^{-1}, Ω is in arcmin^2, and τ_{13} is the

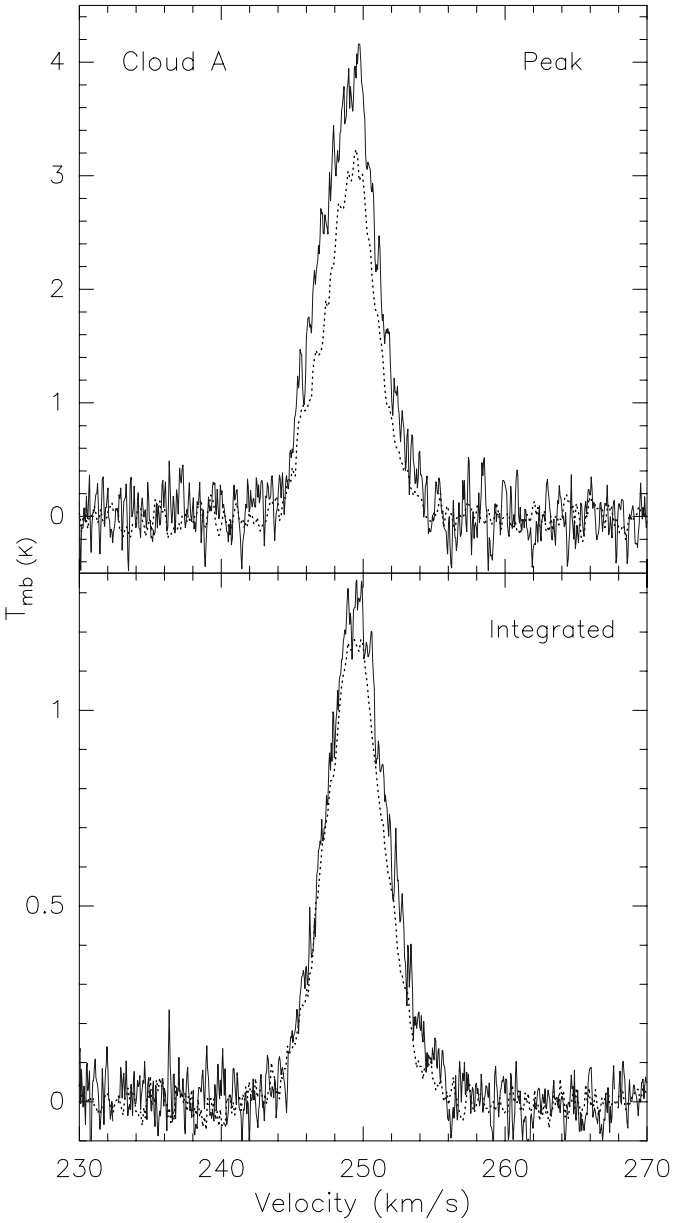

Fig. 8. Spectra of the CO(2→1) (continuous line) and CO(1→0) (dotted line) emission from cloud A. Top: peak spectra. Bottom: integrated spectra.

optical depth of the ^{13}CO(1→0) line. The integral on the right hand side is directly computed from the derived opacity of the ^{13}CO(1→0) line (see Sect. 4.2) and observed line width at each position within a cloud. We find that the LTE masses of Complex-37 clouds computed using the Galactic value of the [$H_2/^{13}$CO] abundance ratio of 7×10^5 (Dickman 1978; Solomon et al. 1979), are in average a factor of 2.5 smaller than the virial masses. This suggests that in this region of the LMC the [$H_2/^{13}$CO] abundance ratio is 2.5 times greater than the Galactic value, or [$H_2/^{13}$CO] = 1.8×10^6. This value is similar to that derived by Heikkilä et al. (1999) toward the N159W region of the LMC. The LTE masses of clouds, computed from Eq. (3) assuming $T_{\rm ex} = 10$ K and [$H_2/^{13}$CO] = 1.8×10^6 are given in Col. 4 of Table 5.

4.2. Optical depths

The ^{12}CO to ^{13}CO ratio of peak intensity can be used to estimate the optical depth of the emission provided the [^{12}CO/^{13}CO] abundance ratio is known. Assuming that the excitation temperature of the $J = 1 \rightarrow 0$ lines and that the surface filling factors of the ^{12}CO and ^{13}CO emissions are equal, the ratio of brightness temperature, $\mathcal{R}$, is given by

$$\mathcal{R}\left(\frac{^{12}\mathrm{CO}}{^{13}\mathrm{CO}}\right) = \left\{\frac{1-\exp(-\tau_{10}^{12})}{1-\exp(-\tau_{10}^{13})}\right\}\left\{\frac{J_{10}^{12}(T_{\rm ex}) - J_{10}^{12}(T_{\rm bg})}{J_{10}^{13}(T_{\rm ex}) - J_{10}^{13}(T_{\rm bg})}\right\}, \quad (4)$$

where τ is the optical depth, $T_{\rm ex}$ is the excitation temperature, $T_{\rm bg}$ is the background radiation temperature, and

$$J_\nu(T) = \frac{h\nu}{k}\frac{1}{[\exp(h\nu/kT) - 1]}. \quad (5)$$

Superscripts 12 and 13 refers to the ^{12}CO and ^{13}CO isotopes, respectively. The ratio of optical depths is given by

$$\frac{\tau_{10}^{12}}{\tau_{10}^{13}} = a\left(\frac{1-\exp(-h\nu_{10}^{12}/kT_{\rm ex})}{1-\exp(-h\nu_{10}^{13}/kT_{\rm ex})}\right)\left\{\frac{kT_{\rm ex}/hB^{13} + 1/3}{kT_{\rm ex}/hB^{12} + 1/3}\right\}, \quad (6)$$

where a is the [^{12}CO/^{13}CO] abundance ratio, and B is the rotation constant of the molecule. In addition, this approach implicitly assumes an homogeneous medium with a plane parallel geometry, probably a too simplistic situation. As shown by Spaans & van Dishoeck (1997) and Pagani (1998), geometrical effects and inhomogeneous density distribution may play an important role in the computed line intensities. In spite of these caveats, we give in Cols. 5 and 6 of Table 5 the optical depths in the ^{13}CO(1→0) and ^{12}CO(1→0) lines, respectively, of the clouds within Complex-37 derived assuming $a = 25$ (Heikkilä et al. 1999) and $T_{\rm ex} = 10$ K. We also computed opacities assuming an abundance ratio of 50, as derived for Galactic disk clouds. The ^{13}CO(1→0) opacities are typically ∼0.08 showing that the emission in this line is optically thin. The ^{12}CO(1→0) emission is, on the other hand, optically thick, with opacities at the peak positions ranging from 1.6 to 3.2 for $a = 25$ and from 4.0 to 6.7 for $a = 50$. These opacities are remarkably smaller (see also Bolatto et al. 2000) than the typical opacities of molecular clouds in our Galaxy of 20–30 (Larson 1981; Frerking et al. 1982). The column densities of ^{13}CO, computed from the derived ^{13}CO opacities, are given in Col. 7 of Table 5. The average density $n(H_2)$, computed from the ^{13}CO column density assuming that the path length is equal to the derived diameter and using [$H_2/^{13}$CO] = 1.8×10^6, are given in Col. 9 of Table 5. We emphasize that this method gives only a rough estimate of the physical parameters.

4.3. Line widths and velocity fields

The line widths of the CO(1→0) emission from the molecular clouds within Complex-37 are considerable larger than the thermal widths expected for a kinetic temperature of 10 K, of ∼0.05 K. There are many effects which

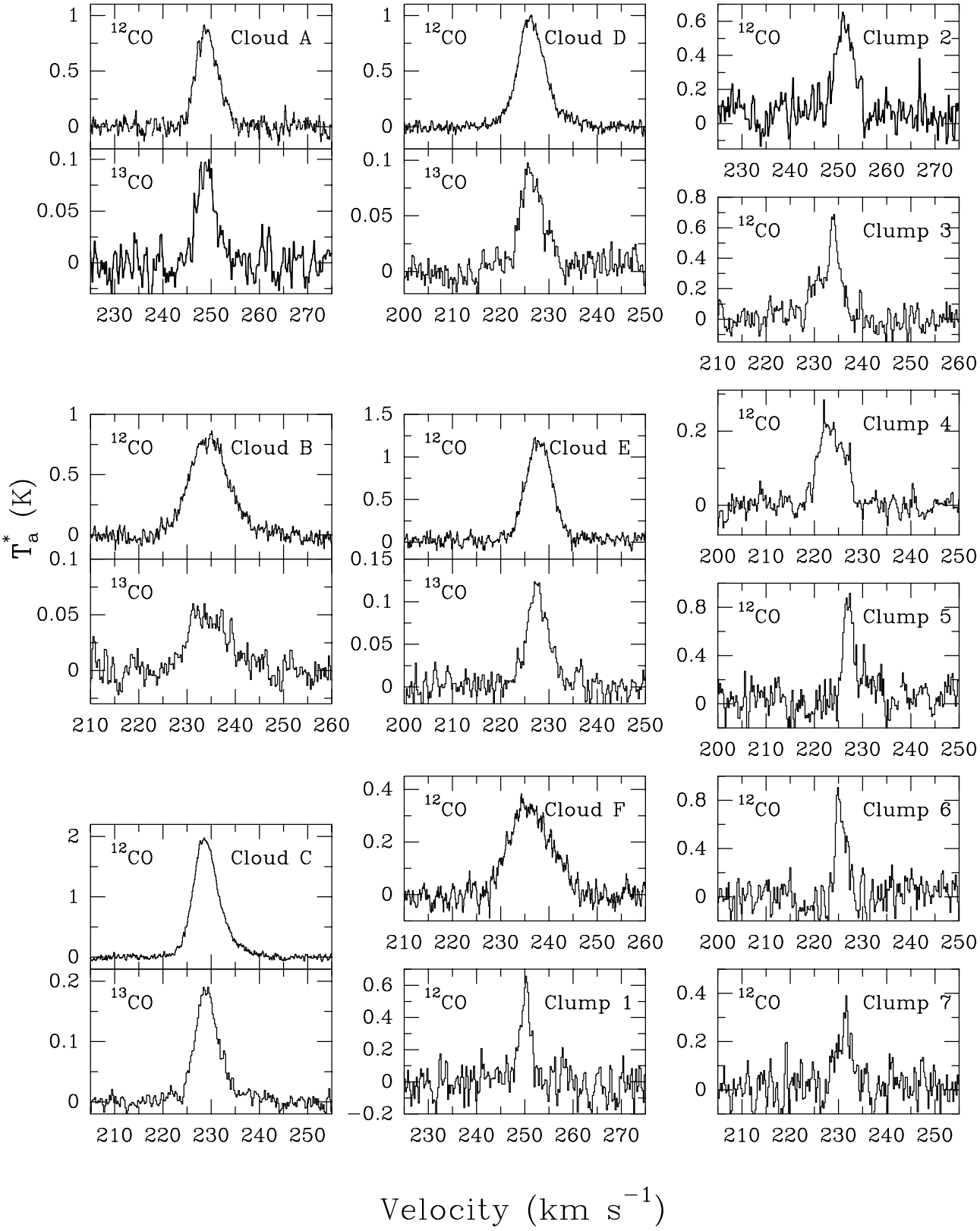

Fig. 9. Average spectra of the CO(1→0) and ^{13}CO(1→0) (when available) line emission from clouds and clumps.

can produce the line broadening, such as bulk motions of the gas, turbulence (cf. Larson 1981; Falgarone & Phillips 1990; Falgarone et al. 1994) and/or magnetic fields (cf. Elmegreen 1990). The contribution of bulk motions to the broadening can be assessed from the observed velocity field. From an inspection of Fig. 4, we conclude that bulk motions of the gas, such as rotation, can produce broadening of only 1–2 km s^{-1}, except for cloud F, and therefore

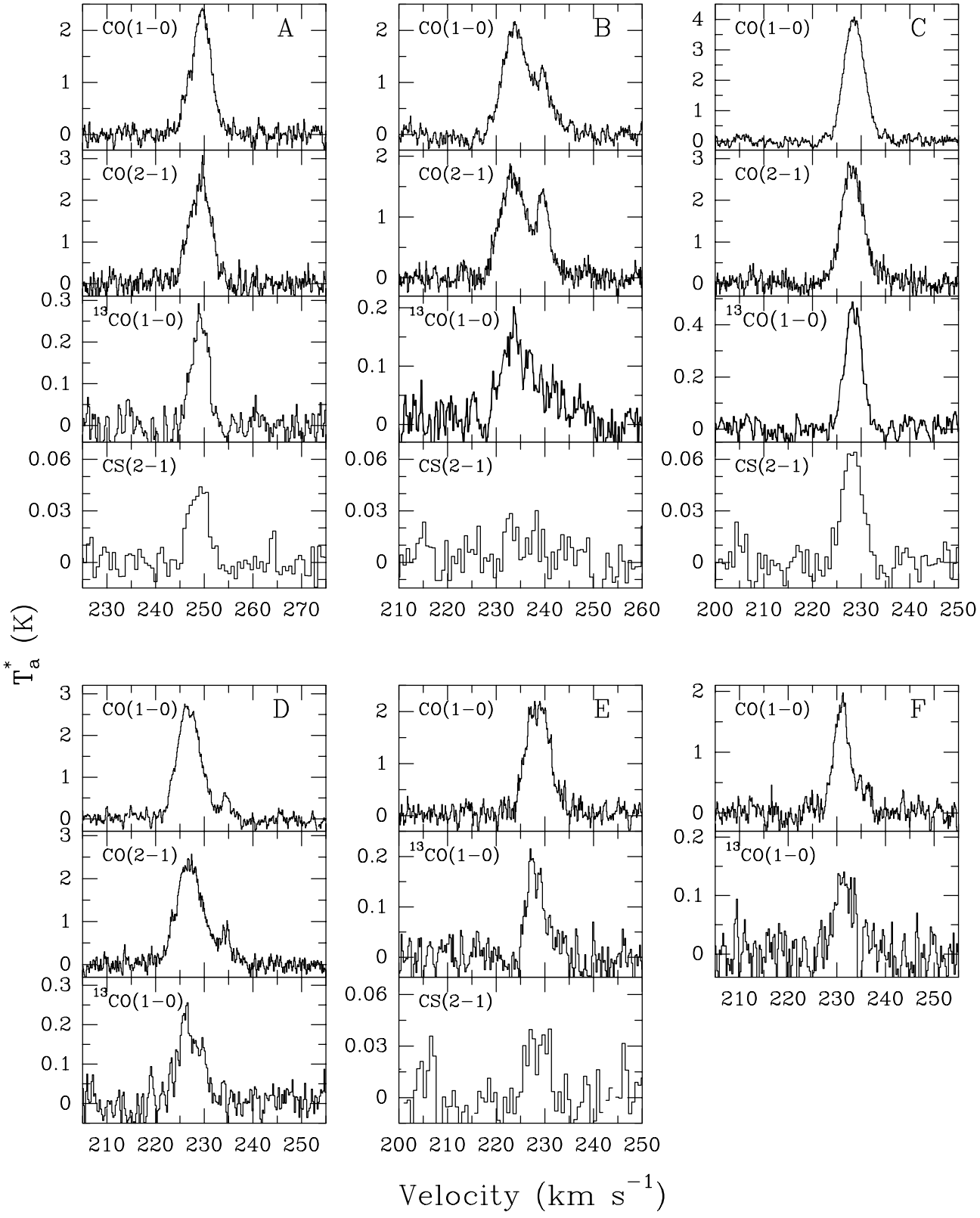

Fig. 10. Spectra of the CO(1→0), CO(2→1), ^{13}CO(1→0), and CS(2→1) emission observed at the peak position of the clouds.

they are unable to explain the observed line widths. Even though the presence of supersonic gas motions in molecular clouds have been known for more than two decades (Zuckerman & Evans 1974), their physical origin is still controversial. Most of the observed characteristics of the line widths have been attributed to turbulent motions, but the physical properties of the turbulence and feeding mechanism are poorly known.

Table 4. Line ratios.

Cloud	Peak ($T_{\rm mb}$)			Integrated ($\int T_{\rm mb}{\rm d}v$)			$\int T_{\rm mb}{\rm d}v{\rm d}\Omega$
	$\frac{\rm CO(2\rightarrow1)}{\rm CO(1\rightarrow0)}$	$\frac{\rm CO(1\rightarrow0)}{^{13}\rm CO(1\rightarrow0)}$	$\frac{\rm CO(2\rightarrow1)}{\rm CS(2\rightarrow1)}$	$\frac{\rm CO(2\rightarrow1)}{\rm CO(1\rightarrow0)}$	$\frac{\rm CO(1\rightarrow0)}{^{13}\rm CO(1\rightarrow0)}$	$\frac{\rm CO(2\rightarrow1)}{\rm CS(2\rightarrow1)}$	$\frac{\rm CO(1\rightarrow0)}{^{13}\rm CO(1\rightarrow0)}$
A	1.24	8.8	53	1.33	11.0	59	11.4
B	0.96	13.4	110	1.10	11.2	135	15.8
C	0.80	8.5	63	0.86	10.4	68	11.4
D	1.03	13.5	–	1.14	12.7	–	14.0
E	–	11.8	65	–	16.9	75	12.9
F	–	12.7	–	–	14.0	–	–

Table 5. Derived parameters.

Name	Masses			Optical depths		Column densities		$n({\rm H_2})$
	$M_{\rm vir}$ ($M_\odot$)	$M_{\rm CO}$ [a] ($M_\odot$)	$M_{\rm LTE}$ ($M_\odot$)	τ_{13}	τ_{12}	$N(^{13}{\rm CO})$ (cm^{-2})	$N({\rm H_2})$ (cm^{-2})	(cm^{-3})
Clouds								
A	1.2×10^5	1.4×10^5	1.7×10^5	0.11	3.1	2.8×10^{15}	5.0×10^{21}	4.2×10^3
B	5.2×10^5	4.6×10^5	2.8×10^5	0.062	1.7	2.6×10^{15}	4.7×10^{21}	2.7×10^3
C	2.3×10^5	7.3×10^5	3.8×10^5	0.12	3.2	3.1×10^{15}	5.6×10^{21}	3.2×10^3
D	2.9×10^5	4.9×10^5	3.3×10^5	0.062	1.7	2.3×10^{15}	4.1×10^{21}	2.2×10^3
E	1.9×10^5	2.8×10^5	2.0×10^5	0.076	2.1	2.0×10^{15}	3.6×10^{21}	2.7×10^3
F	7.2×10^5	3.1×10^5	–	0.068	1.8	1.7×10^{15}	3.1×10^{21}	1.5×10^3
Clumps								
1	1.7×10^4	1.5×10^4	–	–	–	–	–	–
2	4.6×10^4	2.4×10^4	–	–	–	–	–	–
3	2.6×10^4	2.7×10^4	–	–	–	–	–	–
4	1.5×10^5	3.4×10^4	–	–	–	–	–	–
5	2.4×10^4	2.0×10^4	–	–	–	–	–	–
6	1.1×10^4	1.0×10^4	–	–	–	–	–	–
7	4.6×10^4	1.5×10^4	–	–	–	–	–	–

[a] Using a conversion factor of $6.4\times10^{20}{\rm cm^{-2}\ K^{-1}\ km^{-1}\ s}$.

The broader lines are observed toward cloud B, while the largest velocity gradient is observed toward cloud F. This can be appreciated in Fig. 11, which shows position-velocity diagrams along the three lines (L1, L2, and L3) marked in Fig. 1. The question arises as to the nature of the velocity field in clouds B and F. Is there a connection between the structure, morphology, and kinematics of these clouds and identifiable energy sources (expansion of HII regions, supernovae explosions, etc)? Near the northwest border of cloud B lies the extended ($10'\times6'$), filamentary, HII region DEM 304 (also MC86), and projected on its face is the more compact ($1\farcm7\times1\farcm7$) diffuse, shell-like HII region DEM 307. The proximity to regions of ionized gas suggests that cloud B may be experiencing the effects from these well known sources of kinetic energy and turbulence in molecular clouds. Whether the large velocity dispersions in cloud B are due to the presence of an ensemble of smaller clouds or kinematic motions within a single cloud is, however, difficult to assess. Falgarone et al. (1994) computed line profiles of molecular clouds in the case that the main contribution to the gas motions is a turbulent velocity field. The synthetic line profiles show skewness, multiple peaks, wings, and variations from point to point, all of which reflect the intermittency of the velocity field. There is a notable similarity between the line profiles observed toward cloud B and the synthesized profiles, suggesting this object is an extreme turbulent cloud.

The bottom region exhibits more signpost of massive star formation than the top region. Surrounded by cloud F and clumps 3 and 4 lies the HII region DEM 312; projected toward the peak of cloud F are two knots of ionized gas (the compact sources DEM 313 and 314); finally, the supernova remnant DEM 316 (MC 89) lies near the southeast border of cloud F. The observed morphology, association to HII regions, and closeness to a supernova remnant, suggest that cloud F may be undergoing disruption by the mechanical energy and luminosity of the nearby sources. The magnitude of the velocity gradient observed in cloud F is $\sim$1.4 km s^{-1} arcmin^{-1} or 0.087 km s^{-1} pc^{-1}. If due to rotational motions, this gradient will imply a cloud mass of $\sim2\times10^5\ M_\odot$. We feel however that the velocity field observed toward source F is most likely reflecting

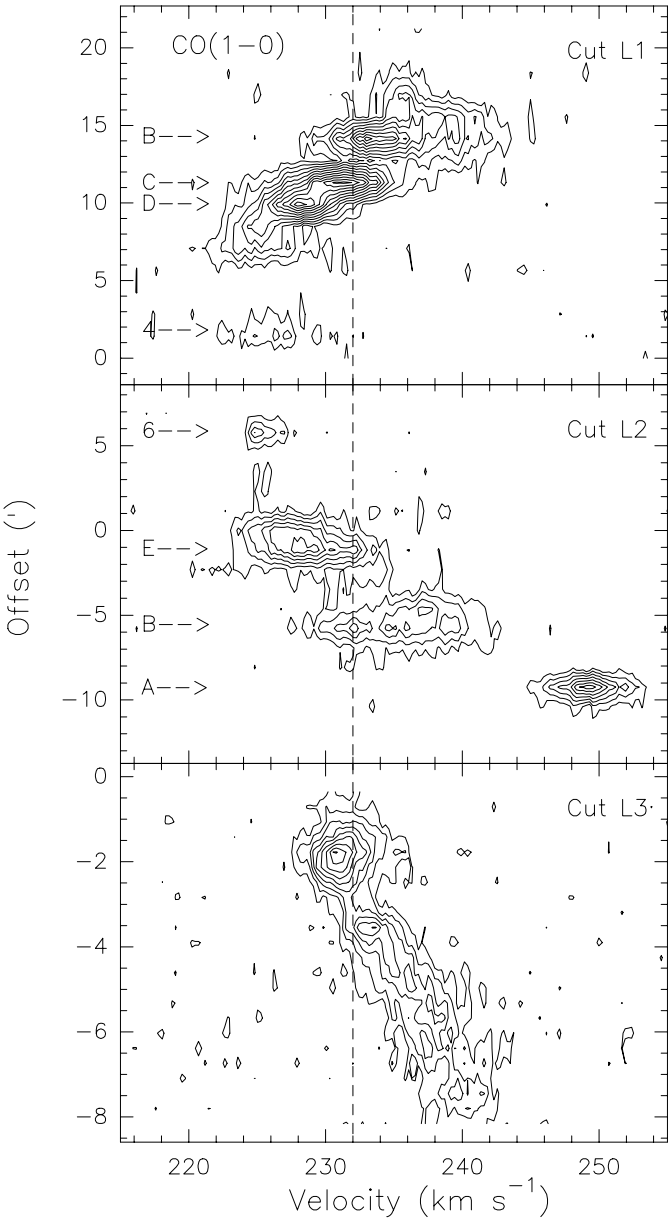

Fig. 11. Position-velocity diagram of the CO(1→0) emission along the cuts shown in Fig. 1. Top: diagram along cut L1. Middle: diagram along cut L2. Bottom: diagram along cut L3. Contour levels are drawn at −0.25 K, and from 0.25 K up in steps of 0.25 K in the top and bottom panels, and at −0.23 K and from 0.23 K up in steps of 0.23 K in the middle panel. The vertical dotted lines indicate the LSR velocity of the HI L-component.

the presence of shocks in molecular clouds in the vicinity of star forming regions and/or supernovae.

4.4. Relationship between parameters of molecular clouds

For molecular clouds in our Galaxy there appears to be a number of relations between observed parameters, such as line width with size and CO luminosity with line width, which are thought to underly fundamental properties of molecular clouds (cf. Blitz 1993, and references therein). The reality, and implications, of these relations have been challenged by several authors, mainly on the basis that Galactic clouds are difficult to define due to blending of spectral lines, the presence of foreground and background emission, and/or the necessity of using kinematic criteria for determining their distances (cf. Issa et al. 1990). Molecular clouds in the LMC are largely free of these observational effects and are thus ideal objects to investigate the authenticity of the correlations derived for Galactic clouds.

4.5. Line width versus size

Figure 12a plots the line width versus size of the clouds and clumps within Complex-37 (filled squares). Also plotted, for comparison, are the sizes of clouds and clumps within the 30 Dor region of the LMC (circles) determined from SEST observations (Johansson et al. 1998). The *FWHM* sizes reported by the later authors were converted to radii multiplying by a factor of 0.8 (cf. Heikkilä et al. 1999). An immediate result is that the clouds and clumps within Complex-37 have larger sizes than those in 30 Dor. We note that even though the methods used to estimate sizes are different, the difference in cloud sizes for the two regions is most likely due to the difference in physical environment between the two regions. The 30 Dor region is associated with several bright HII regions and is characterized by exhibiting strong activity of massive star formation. The small size of the molecular clouds in this region suggests that they are being dissipated by the UV photons from the luminous stars, and/or disrupted by the mechanical energy injected by the massive stars.

In addition, Fig. 12a shows that there is a correlation between line width and size. The existence of a power law relationship between size and line width of molecular clouds in our Galaxy was first pointed out by Larson (1981). A power law index of 1/2 is thought to indicate that molecular clouds are in virial equilibrium. A least-square fit to the trend defined by the clouds and clumps within Complex-37 gives $\Delta v = 0.24\ R^{1.0\pm0.1}$, where Δv is in km s^{-1} and R in pc. As pointed out by Kutner et al. (2002) there is a wide variation in the size-line width relation for molecular clouds in different regions of the LMC. For instance for the clouds in the 30 Dor region a least-square fit gives $\Delta v = 1.0\ R^{0.65\pm0.11}$. Whether the difference in slopes is linked to differences in the physical conditions of each region or produced by the small number of clouds in each region is not yet clear. Note that a least-square fit to the trend defined by combined data set gives $\Delta v = 0.98\ R^{0.61\pm0.07}$.

4.6. Virial mass versus CO luminosity

Figure 12b shows the relation between the virial mass and CO luminosity for the clouds and clumps within Complex-37. A least-square fit to the trend, shown as a

continuous line, gives $M_{\rm vir} = 68.7\ L_{\rm CO}^{0.84\pm0.10}$, where $L_{\rm CO}$ is in K km s^{-1} pc^2 and $M_{\rm vir}$ is in $M_\odot$. Since $L_{\rm CO}$ might be proportional to the mass of the cloud, Fig. 12b may tell us about the conversion factor of clouds in the LMC (or at least in Complex-37). The dotted line represent the relation given by Eq. (2) with $X = 2.3X_{\rm Gal}$, which is in addition coincident with the relationship we derive for outer Galaxy molecular clouds using the data reported by May et al. (1997). We conclude that the conversion factor for clouds in Complex-37 is a factor of 2.3 times larger than that derived for inner Galactic clouds, and similar to that for clouds in the outer Galaxy.

From a comparison of virial and CO masses, Cohen et al. (1988) estimated that the conversion factor is ∼6 times larger than for GMCs in our Galaxy. However as discussed in Sect. 4.1, the virial masses determined from the Columbia observations are largely overestimated, due to the coarse angular resolution, which results in an overestimate of the conversion factor. We conclude that the conversion factor from velocity integrated CO emission to H_2 column density in the LMC is lower than the value found by Cohen et al. (1988) by roughly a factor of 3.

4.7. The relationship between CO and HI

The spectra of the HI emission toward Complex-37 shows the presence of two velocity components, with LSR central velocities of ∼234 and 271 km s^{-1} near the top region and ∼230 and 280 km s^{-1} near the bottom region (Rohlfs et al. 1984). These components are thought to trace two separate structural features: the high velocity gas a disk (D) HI component and the low velocity gas a surface (L) HI component (Luks & Rohlfs 1992). The center velocities of the molecular clouds within Complex-37 are in all cases closer to the low velocity than to the high velocity HI component, indicating that the molecular clouds within Complex-37 are associated only with the L component, no CO emission being detected associated with the D component.

The question arises as to why molecular clouds are formed only within the L component. Whereas the HI column densities of the D and L components toward Complex-37 are quite similar, of $\sim 1.5 \times 10^{21}$ cm^{-2}, the velocity dispersion of the D component is 2 to 3 times larger than that of the L component. This shows that the disk component is considerable more turbulent, possible due to the effects of a strong radiation field and shocks from powerful stellar winds. We suggest that, in the direction of Complex-37, the L-component is exposed to a much lower radiation field than the D component, with the UV radiation penetrating only the skin of this HI cloud and allowing the formation of H_2 molecules in their interior. This hypothesis is supported by Fig. 3 of Snowden & Petre (1994; see also Fig. 1 of Blondiau et al. 1997), which shows that there is a strong attenuation in the extended X-ray emission at the position of Complex-37. The shadowing of the X-ray emission indicates that Complex-37 is located in front of the diffuse X-ray emission associated with the disk HI component, and away from sources of strong disruption and turbulence.

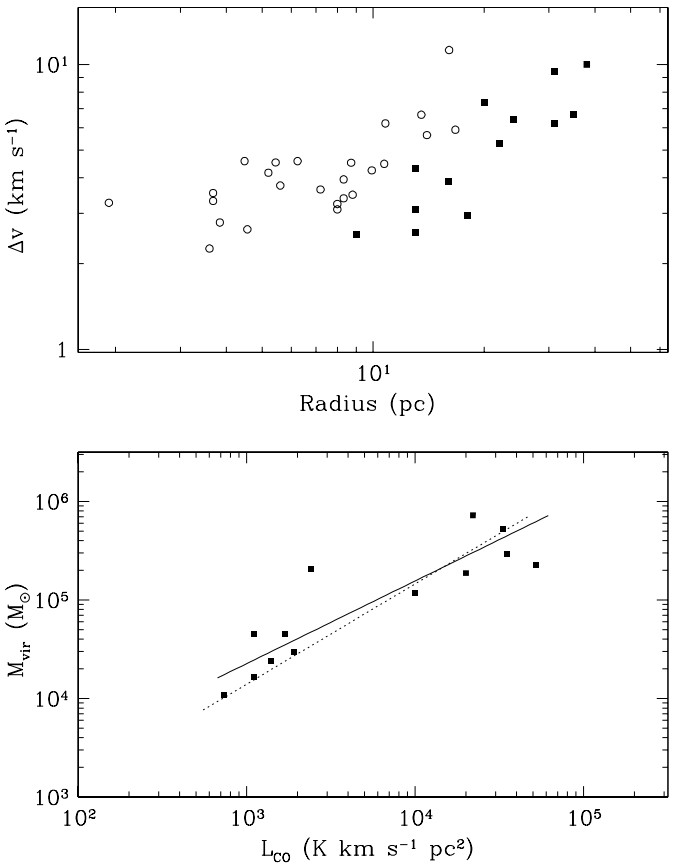

Fig. 12. Upper panel: line width versus radius for clouds and clumps within Complex-37 (filled squares) and clouds and clumps within the 30 Doradus region (open circles; Johansson et al. 1998). Lower panel: virial mass versus CO luminosity for clouds and clumps within Complex-37 (filled squares). The continuous line corresponds to a least squares fit to the data. The dotted line corresponds to Eq. (2) with $X = 2.3X_{\rm Gal}$, which coincides with the relationship derived for molecular clouds in the outer Galaxy (May et al. 1997).

5. Summary

We made observations, with linear resolutions of ∼10 pc using SEST, of the CO(1→0), CO(2→1) and ^{13}CO(1→0) line emission from the giant molecular complex No. 37 of the Large Magellanic Cloud. The main results and conclusions presented in this paper are summarized as follows.

The CO(1→0) emission arises from six large, distinct, clouds, with sizes ranging from 22 to 38 pc, and seven smaller clumps, with sizes ranging from 9 to 16 pc. The CO luminosities of the clouds range from 1×10^4 to 5×10^4 K km s^{-1} pc^2 and those of the clumps from 7×10^2 to 2×10^3 K km s^{-1} pc^2. The CO(1→0) opacities at the peak position of the clouds are remarkably smaller than those derived for Galactic molecular clouds, being in the range between 1.6 to 3.2 or 4.0 to 6.7 for a [CO/^{13}CO] abundance ratio of 25 and 50, respectively.

The virial mass of clouds and clumps are typically 3×10^5 $M_\odot$ and 3×10^4 $M_\odot$, respectively. The molecular hydrogen column densities and densities of the clouds are typically 5×10^{21} cm^{-2} and 3×10^3 cm^{-3}, respectively.

The total CO luminosity of the complex determined from the SEST observations is 1.8×10^5 K km s^{-1} pc^2, which is in excellent agreement with that determined from the low spatial resolution (∼140 pc) observations of Cohen et al. (1988). This shows that there is little diffuse CO emission outside the clouds. The total mass of molecular gas in the complex derived from the SEST observations, assuming that the individual clouds are virialized, is 2.4×10^6 $M_\odot$, which is a factor of 6 lower than that estimated by Cohen et al. under the same assumption. We conclude that the determination of the velocity integrated CO emission to H_2 column density conversion factor in the LMC from low angular resolution observations has been overestimated by a factor of ∼3. From the virial mass versus CO luminosity relationship we estimate that the conversion factor for clouds in Complex-37 is similar to that derived for clouds in the outer Galaxy, and a factor of 2–3 larger than that derived for clouds in the inner Galaxy.

Acknowledgements. G.G. gratefully acknowledges support from the Chilean Fondecyt Project 1010531.

References

Blitz, L. 1993 in Protostars and Planets III, ed. E. H. Levy, & J. I. Lunine (Tucson: University of Arizona), 125
Blondiau, M. J., Kerp, J., Mebold, U., & Klein, U. 1997, A&A, 323, 585
Bolatto, A., Jackson, J. M., Israel, F. P., Zhang, X., & Kim, S. 2000, ApJ, 545, 234
Bourke, T. L., Garay, G., Lehtinen, K. K., et al. 1997, ApJ, 476, 781
Cohen, R. S., Dame, T. M., Garay, G., et al. 1988, ApJ, 331, L95
Combes, F. 1991, ARA&A, 29, 195
Dame, T. M., Elmegreen, B. G., Cohen, R. S., & Thaddeus, P. 1986, ApJ, 305, 892
Dame, T. M., Hartmann, D., & Thaddeus, P. 2001, ApJ, 547, 792
Davies, R. D., Elliott, H. K., & Meaburn, J. 1976, MNRAS, 81, 89
Dickel, J. R., & Milne, D. K. 1994, Pub. Ast. Soc. Austr., 11, 99
Dickman, R. L. 1978, ApJS, 37, 407
Digel, S. W., Aprile, E., Hunter, S. D., Mukherjee, R., & Xu, C. 1999, ApJ, 520, 196
Digel, S. W., Grenier, I. A., Heithausen, A., Hunter, S. D., & Thaddeus, P. 1996, ApJ, 463, 609
Elmegreen, B. G. 1990, ApJ, 361, L77
Falgarone, E., & Phillips, T. G. 1990, ApJ, 359, 344
Falgarone, E., Lis, D. C., Phillips, T. G., et al. 1994, ApJ, 436, 728
Filipovic, M. D., Haynes, R. F., White, G. L., et al. 1995, A&AS, 111, 311
Frerking, M. A., Langer, W. D., & Wilson, R. W. 1982, ApJ, 262, 590
Garnett, D. R. 1999, New Views of the Magellanic Clouds, IAU Symp. 190, ed. Y.-H. Chu, N. Suntzeff, J. E. Hesser, & D. A. Bohlender, 266
Heikkilä, A., Johansson, L. E. B., & Olofsson, H. 1999, A&A, 344, 817
Hunter, S. D., Bertsch, D. L., Catelli, J. R., et al. 1997, ApJ, 481, 205
Israel, F. P. 1997, A&A, 328, 471
Israel, F. P., Maloney, P. R., Geis, N., et al. 1996, ApJ, 465, 738
Issa, M., MacLaren, I., & Wolfendale, A. W. 1990, ApJ, 352, 132
Johansson, L. E. B., Olofsson, H., Hjalmarson, A., Gredel, R., & Black, J. H. 1994, A&A, 291, 89
Johansson, L. E. B., Greve, A., Booth, R. S., et al. 1998, A&A, 331, 857
Koornneef, J. 1982, A&A, 107, 247
Kutner, M. L., & Ulich, B. L. 1981, ApJ, 250, 341
Kutner, M. L., Rubio, M., Booth, R. S., et al. 1997, A&AS, 122, 255
Kutner, M. L., Rubio, M., Garay, G., et al. 2002, in preparation
Larson, R. B. 1981, MNRAS, 194, 809
Lequeux, J. 1989, in Recent Developments of Magellanic Cloud Research, ed. K. S. de Boer, F. Spite, & G. Stasinska (Paris: Obs. Paris), 119
Lequeux, J., Le Bourlot, J., des Forets, G. P., et al. 1994, A&A, 292, 371
Luks, Th., & Rohlfs, K. 1992, A&A, 263, 41
MacLaren, I., Richardson, K. M., & Wolfendale, A. W. 1988, ApJ, 333, 821
Mathewson, D. S., Ford, V. L., Dopita, M. A., et al. 1983, ApJS, 51, 345
May, J., Alvarez, H., & Bronfman, L. 1997, A&A, 327, 325
McGee, R. X., Brooks, J. W., & Batchelor, R. A. 1972, Austr. J. Phys., 25, 581
Mochizuki, K., Nakagawa, T., Doi, Y., et al. 1994, ApJ, 430, L37
Pagani, L. 1998, A&A, 333, 269
Polk, K. S., Knapp, G. R., Stark, A. A., & Wilson, R. W. 1988, ApJ, 332, 432
Rohlfs, K., Kreitschmann, J., Feitzinger, J. V., & Siegman, B. C. 1984, A&A, 137, 343
Rubio, M., & Garay, G. 1988, in Molecular Clouds in the Milky Way and External Galaxies, ed. R. L. Dickman, R. L. Snell, & J. S. Young (Springer: Verlag), 426
Rubio, M., Lequeux, J., & Boulanger, F. 1993, A&A, 271, 9
Scoville, N. Z., & Sanders, D. B. 1987, in Interstellar Processes, ed. D. J. Hollenbach, & H. A. Thronson (Reidel: Dordrecht), 21
Snowden, S. L., & Petre, R. 1994, ApJ, 436, L123
Solomon, P. M., Scoville, N. Z., & Sanders, D. B. 1979, ApJ, 232, L89
Solomon, P. M., Rivolo, A. R., Barrett, J., & Yahil, A. 1987, ApJ, 319, 730
Spaans, M., & van Dishoeck, E. F. 1997, A&A, 323, 953
Strong, A. W., Bloemen, J. B. G. M., Dame, T. M., et al. 1988, A&A, 207, 1
Tumlinson, J., Shull, J. M., Rachford, B. L., et al. 2001, ApJ, submitted
Zuckerman, B., & Evans, N. J. II 1974, ApJ, 192, L149